



## Research

**Cite this article:** Mengüç Y, Röhrig M, Abusomwan U, Hölscher H, Sitti M. 2014 Staying sticky: contact self-cleaning of gecko-inspired adhesives. *J. R. Soc. Interface* **11**: 20131205.  
<http://dx.doi.org/10.1098/rsif.2013.1205>

Received: 28 December 2013

Accepted: 28 January 2014

### Subject Areas:

biomimetics

### Keywords:

adhesion, gecko, self-cleaning, contact, micro-fibre

### Author for correspondence:

Metin Sitti  
e-mail: [sitti@cmu.edu](mailto:sitti@cmu.edu)

†These authors contributed equally to this study.

# Staying sticky: contact self-cleaning of gecko-inspired adhesives

Yiğit Mengüç<sup>1,†</sup>, Michael Röhrig<sup>2,†</sup>, Uyiosa Abusomwan<sup>1,†</sup>, Hendrik Hölscher<sup>2</sup> and Metin Sitti<sup>1</sup>

<sup>1</sup>Department of Mechanical Engineering, Carnegie Mellon University, Pittsburgh, PA 15213, USA

<sup>2</sup>Institute of Microstructure Technology, Karlsruhe Institute of Technology (KIT), 76344 Eggenstein-Leopoldshafen, Germany

The exceptionally adhesive foot of the gecko remains clean in dirty environments by shedding contaminants with each step. Synthetic gecko-inspired adhesives have achieved similar attachment strengths to the gecko on smooth surfaces, but the process of contact self-cleaning has yet to be effectively demonstrated. Here, we present the first gecko-inspired adhesive that has matched both the attachment strength and the contact self-cleaning performance of the gecko's foot on a smooth surface. Contact self-cleaning experiments were performed with three different sizes of mushroom-shaped elastomer microfibres and five different sizes of spherical silica contaminants. Using a load–drag–unload dry contact cleaning process similar to the loads acting on the gecko foot during locomotion, our fully contaminated synthetic gecko adhesives could recover lost adhesion at a rate comparable to that of the gecko. We observed that the relative size of contaminants to the characteristic size of the microfibres in the synthetic adhesive strongly determined how and to what degree the adhesive recovered from contamination. Our approximate model and experimental results show that the dominant mechanism of contact self-cleaning is particle rolling during the drag process. Embedding of particles between adjacent fibres was observed for particles with diameter smaller than the fibre tips, and further studied as a temporary cleaning mechanism. By incorporating contact self-cleaning capabilities, real-world applications of synthetic gecko adhesives, such as reusable tapes, clothing closures and medical adhesives, would become feasible.

## 1. Introduction

Geckos have the striking ability to keep their toes sticky and clean through contact self-cleaning. This impressive characteristic is counterintuitive at first sight because it does not match our everyday experience with sticky materials. Commonplace office tape loses its adhesion strength after contamination and cannot recover it through mechanical means (figure 1). Geckos, on the other hand, are able to run along walls and ceilings even in 'dirty' habitats such as jungles or deserts. Consequently, it is of great interest to understand the mechanics behind the self-cleaning process in geckos. During the past decades, engineers and scientists successfully uncovered the principles of the gecko's impressive adhesive capabilities [1–6], but there are only a few studies on their self-cleaning abilities [7,8]. Although, gecko-inspired adhesives have been demonstrated to compare favourably with the gecko in attachment strength on smooth dry surfaces [9–23], no synthetic gecko adhesive [24–27] has matched its natural counterpart in the ability to regain adhesion after contamination. Consequently, the development of gecko-inspired adhesives with self-cleaning capability is the critical next step to successfully produce biomimetic solutions such as strong and reusable adhesive tapes, power-efficient and robust climbing robots [28,29], and robotic pick-and-place manipulators for tiny parts and large fragile devices [30,31]. One particularly important potential application is in reusable and non-irritating medical bandages [16], but this application also requires a self-cleaning feature to become practical [32].

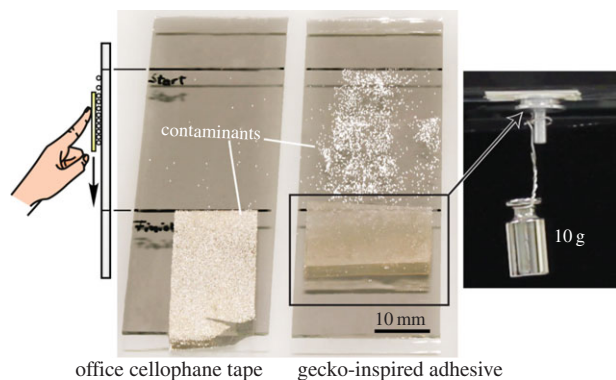


**Figure 1.** The photographs show that the gecko-inspired adhesive shed much of the contaminating particles (white specks) while the Tesafilm commonplace office tape remained fully contaminated after a single contact cleaning cycle. The fibrillar adhesive was able to release nearly all of its contaminants and regained an adhesive strength of 0.87 kPa after shearing, whereas the cellophane tape remained highly contaminated and was unable to hold up its own weight. (Online version in colour.)

Contaminated gecko toes have previously been shown to recover 35% of their initial adhesion after eight artificial steps involving a load–drag–unload cleaning procedure [8]. Such contact-based self-cleaning becomes even more effective if the geckos are allowed to apply their famous digital hyperextension ability. In this case, they are able to recover 80% of initial adhesion strength after only four natural steps [7]. For comparison, the most successful synthetic adhesive, so far, that has demonstrated contact self-cleaning (i.e. load–drag–unload cleaning procedure on dry, rigid, non-adhesive substrates such as glass) recovered only 33% of its initial attachment strength after 30 simulated steps [25]. The initial clean adhesive strength of this adhesive was 8 kPa in shear, which is only 4% of the gecko's adhesive strength [33]. Subsequently, the same synthetic adhesive was placed on a unique loop-shaped backing material and demonstrated full shear adhesion recovery and adhesive strength of nearly 140 kPa in shear [26]. In this work, we show the mechanics of contact self-cleaning of a synthetic gecko-inspired adhesive that combines high adhesive strength with a remarkable adhesion recovery using dry contact self-cleaning. As demonstrated in figure 1, this feature is in contrast to a commercial adhesive tape, which only provides high adhesive strength at first and fails completely after contamination. Furthermore, contact self-cleaning is not effective in the commercial adhesive tape (figure 1). By analysing several size combinations of microfibrils and contaminating particles, we present three regimes of contact self-cleaning mechanics, based on the relative size of the particle to the microfibrils' tip. Using a theoretical model, we explain the essential role of particle rolling or sliding to contact self-cleaning in gecko-inspired adhesives. Finally, we improve the contact self-cleaning capabilities of the adhesives through a structural design inspired by the folds of skin beneath the gecko's adhesive fibrillar structures, called lamellae.

## 2. Material and methods

Polyurethane elastomer microfibrils with mushroom-shaped tips were fabricated using a previously published lithographic technique combined with a post-processing that involved dipping and soft mould casting [34]. Three different sizes of microfibrils with tip diameters,  $B$ , of 20, 30 and 95  $\mu\text{m}$  (figure 2) were fabricated along with a flat unstructured reference sample. The polyurethane

(ST-1060, BJB Enterprises) had a Young's modulus  $E_f$  of 2.9 MPa and a work of adhesion  $W_{pf}$  (to glass) of 93  $\text{mJ m}^{-2}$ . The adhesive samples, including the reference sample, were cut into square patches of  $500 \times 500 \mu\text{m}$  and affixed to a clear acrylic sheet with a double-sided adhesive tape. During the cutting of the patches, structures near the edges were occasionally damaged, but these errors were corrected by our analysis protocol which normalized all self-cleaning results to the initial adhesion of each sample.

In the experiments, glass microspheres with diameters ranging from 3 to 215  $\mu\text{m}$  were used as contaminants (figure 2). The spheres used include: size A (mean diameter,  $D$ , = 2.8  $\mu\text{m}$  with standard deviation,  $D_s$ , = 1.7  $\mu\text{m}$ ; MO-SCI Specialty Products, GL-0191 1–15  $\mu\text{m}$ ); size B ( $D$  = 46.2  $\mu\text{m}$ ,  $D_s$  = 5.8  $\mu\text{m}$ ; Cospheric, SLGMS 45–53  $\mu\text{m}$ ); size C ( $D$  = 118.5  $\mu\text{m}$ ,  $D_s$  = 18.1  $\mu\text{m}$ ; Sartorius, BBI-8541400); size D ( $D$  = 123.6  $\mu\text{m}$ ,  $D_s$  = 26.5  $\mu\text{m}$ ; Sartorius, BBI-8541507); and size E ( $D$  = 213.6,  $D_s$  = 28.9; Potters Industries, type 1922). The mean diameters and standard deviations of the microspheres were determined by analysing the microscopic images of the spheres using customized software. The microspheres were packed in dry air by the supplier and used as supplied. Commercially pre-cleaned glass slides (microscope slide; Pearl) were used as substrates. Prior to using the glass slides, they were first wiped with lint-free lens paper and blasted with compressed air.

Contamination of the samples was achieved by bringing each sample into contact with a monolayer of glass spheres at a speed of 25  $\mu\text{m s}^{-1}$  until a predefined compressive load was reached (10 mN (40 kPa) for small adhesive samples, 15 mN (60 kPa) for medium adhesive samples and 50 mN (200 kPa) for large adhesive samples). The sample was then retracted at the same speed as the loading speed. A disperse monolayer of glass spheres was created using one of the following three approaches depending on the size of the microspheres: for microspheres with  $D > 150 \mu\text{m}$ , it was sufficient to manually pour them onto a glass slide, where they settled through gravity into a monolayer; microspheres with  $15 \mu\text{m} < D < 150 \mu\text{m}$  were first poured onto a glass slide, and then pressed with a glass coverslip to create a monolayer; for microspheres with  $D < 15 \mu\text{m}$ , an aluminium surface was first dusted with the spheres, next a glass slide was electrostatically charged by rubbing it with a piece of lint-free lens paper and the charged glass slide was brought near the dusted surface until the spheres were attracted to the glass slide.

The experimental set-up (figure 3) consists of a three-axis custom-built automated system that was mounted onto an inverted optical microscope (Eclipse LE200; Nikon). The testing system includes linear stages (MFA-CC and VP-25XA; Newport) that were used to move the adhesive sample in the  $z$ -direction for normal loading, and in the  $y$ -direction for shear loading. The normal force applied to the adhesive sample was captured using a load cell and a signal amplifier (GSO-50 and TMO-2; Transducer Techniques) and transferred via a data acquisition board (NI PCI-6259; National Instruments) to a computer. A coloured digital video camera (DFW-X710; Sony) was mounted onto the microscope and used to capture the visual information during the experiment. Customized software was used to control the system and to record time-stamped visual and force data. Proper alignment of the two contacting surfaces was achieved using two manually adjusted rotational stages (GON40-U; Newport) for rotation about the  $x$ - and  $y$ -axis.

Adhesion (pull-off force) measurements were carried out under normal loading by first compressing each sample against the glass substrate until a desired force, known as the preload, was reached. Next, the sample was pulled away perpendicular to the substrate until it broke contact with the substrate. The preload used in the experiments was 10 mN (40 kPa) for small adhesive samples, 15 mN (60 kPa) for the medium adhesive samples and 50 mN (200 kPa) for the large adhesive samples. These preload values were chosen to maximize the attachment force and were determined by analysing the adhesion for a wide range of preloads.

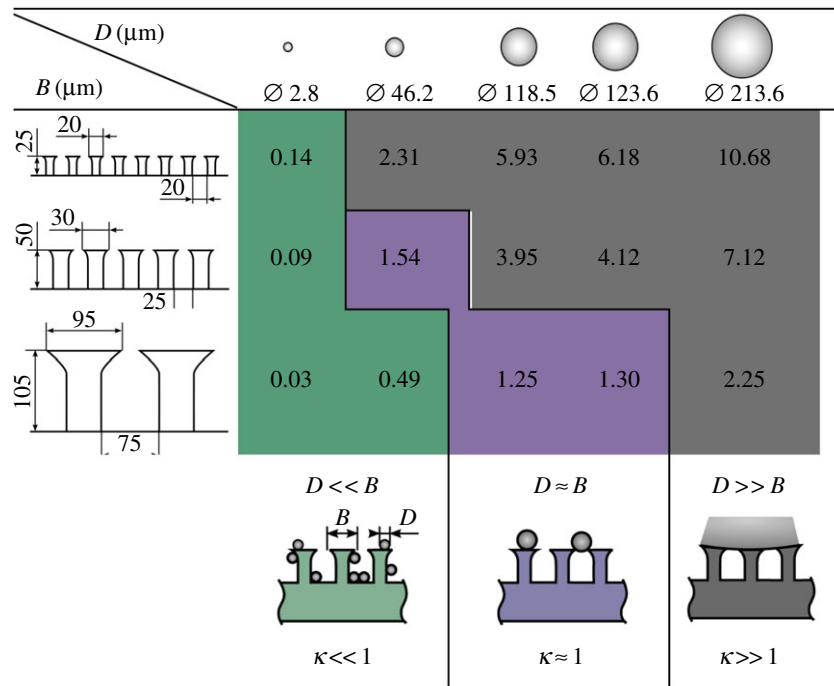


**Figure 2.** Dimensions of the elastomer fibrillar adhesive samples and contaminating microspheres that were used in the experiments. The samples were grouped into small ( $\kappa \ll 1$ ), intermediate ( $\kappa \approx 1$ ) and large ( $\kappa \gg 1$ ) contaminants regimes (table 1).  $B$  is the fibre tip diameter,  $D$  is the mean particle diameter and  $\kappa = D/B$ . (Online version in colour.)

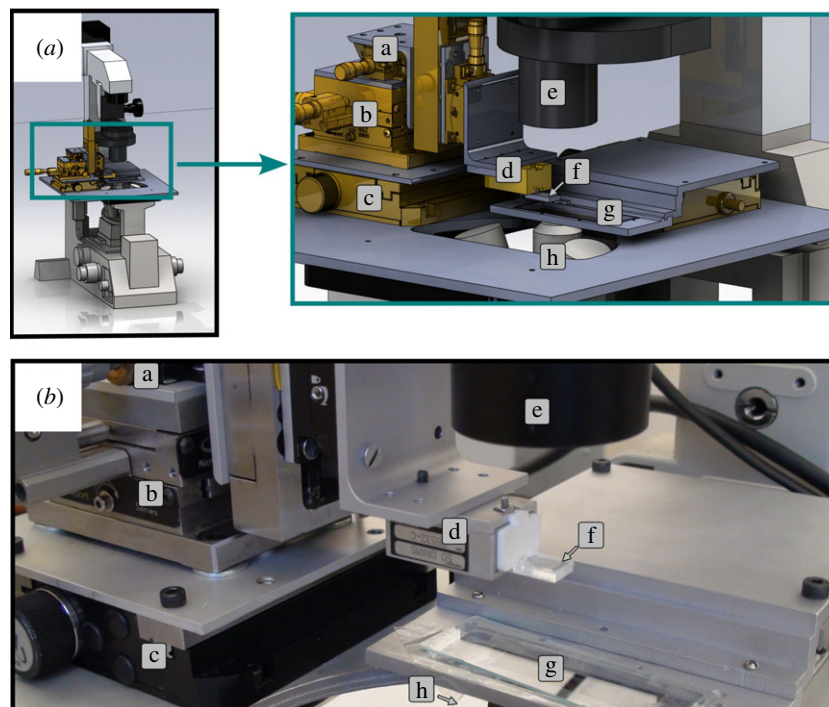


**Figure 3.** The experimental set-up. (a) Rendered model of the adhesion testing system mounted on an inverted view microscope. (b) Photograph of the actual testing system with the various components: a, goniometer ( $x$ - and  $y$ -axis rotational alignment); b, manual  $x$ - and  $y$ -axis stages; c, motorized  $y$ -axis stage; d, load cell; e, light source; f, adhesive sample; g, glass substrate; h, microscope objective. (Online version in colour.)

The contaminated samples were cleaned using a load–drag–unload procedure. First, the sample was compressed (*load*) against a glass substrate at a rate of  $25 \mu\text{m s}^{-1}$  until a desired preload of 100 mN (400 kPa) was reached. Next, the glass substrate was laterally displaced (*drag*) at constant preload for  $750 \mu\text{m}$  at a speed of  $50 \mu\text{m s}^{-1}$ . Finally, the sample was retracted (*unload*) at  $25 \mu\text{m s}^{-1}$  until there was no contact with the substrate. Each cleaning cycle was carried out on a clean section of the glass substrate. Apart from the specified preload, three

samples were cleaned with lower preloads to test the sensitivity of the cleaning performance to this parameter: two samples of small-sized structures were cleaned at a preload of 20 mN (80 kPa), and a patch of medium-sized structures was cleaned at a preload of 30 mN (120 kPa). Qualitatively and quantitatively, these adhesive samples were equivalent in their self-cleaning performance and were as a result included in the test results.

The entire cleaning experiments were conducted in the following procedure as shown in figure 4a: first, the initial

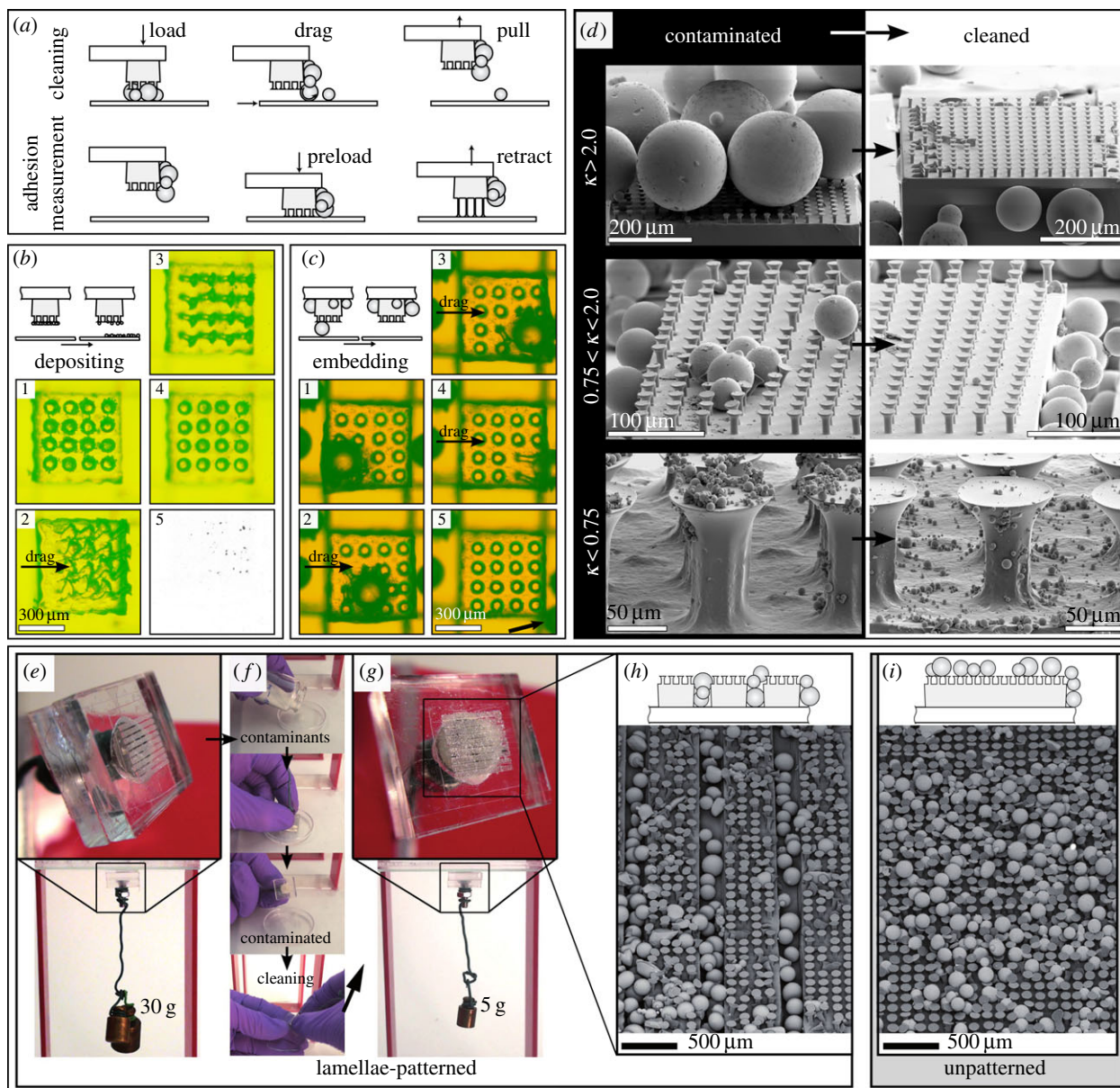


**Figure 4.** Dry contact cleaning images for gecko-inspired fibrillar adhesives. (a) Schematics of the experimental procedure showing the cleaning cycle (load–drag–pull) followed by adhesion measurement (preload–retract). The arrows indicate the direction of motion. (b) Particle deposition during a cleaning cycle for an adhesive sample in the small contaminants regime. The sample is loaded in frame 1, sheared in frames 2 and 3 and unloaded in frame 4. Frame 5 shows the contaminants deposited during the cleaning cycle. (c) Particle rolling and embedding for a sample in the large contaminants regime. (d) Scanning electron microscopy (SEM) images of samples in the three contaminants regimes before and after dry self-cleaning. (e) A non-contaminated lamellae-patterned adhesive patch mounted onto a rigid acrylic backing and holding 30 g of mass ( $\sim 10$  kPa). (f) Contamination and cleaning procedure for the lamellae-patterned adhesive sample. (g) The lamellae-patterned adhesive holding up a load of 5 g ( $\sim 1.7$  kPa) after cleaning. (h) An SEM image of the cleaned lamellae-patterned sample with most of the contaminants embedded in the grooves. The image also shows some microfibrils that have been damaged by the manual cleaning of the lamellae-patterned sample. (i) An SEM image of a non-patterned sample shows a significant amount of contaminants in the array even after cleaning. (Online version in colour.)

adhesive force of a clean sample was measured and recorded as the *clean adhesion*. Second, the sample was contaminated by bringing it into contact with a monolayer of glass spheres. Third, the adhesive force of the sample was measured immediately after contamination, and recorded as the *contaminated adhesion*. Fourth, the sample was cleaned against a glass substrate using a load–drag–unload procedure. In the fifth step, the adhesion of the sample was measured again after cleaning. Finally, the fourth and fifth steps were repeated successively with alternating drag directions. An alternating drag direction was used to prevent possible fibre fatigue and failures of the double-sided adhesive tape used to attach the sample to the testing apparatus. Although the alternating drag direction does not mimic the motion of the natural gecko foot, the cleaning mechanics is not altered, because our synthetic adhesive is

non-directional, unlike the gecko. Following this procedure, a total of 1040 experiments were performed on 24 adhesive samples ( $500 \times 500 \mu\text{m}$  patches). The glass substrate was cleaned as needed by wiping with a dry piece of lens paper and blasting with compressed air.

### 3. Results and discussions

Results from the experiments in figures 4 and 5 show significant cleaning for all samples. The performance of each cleaning cycle was rated by the *relative adhesion*, which is the measured adhesion after the cleaning cycle as a percentage of the *clean adhesion* measured before contamination.

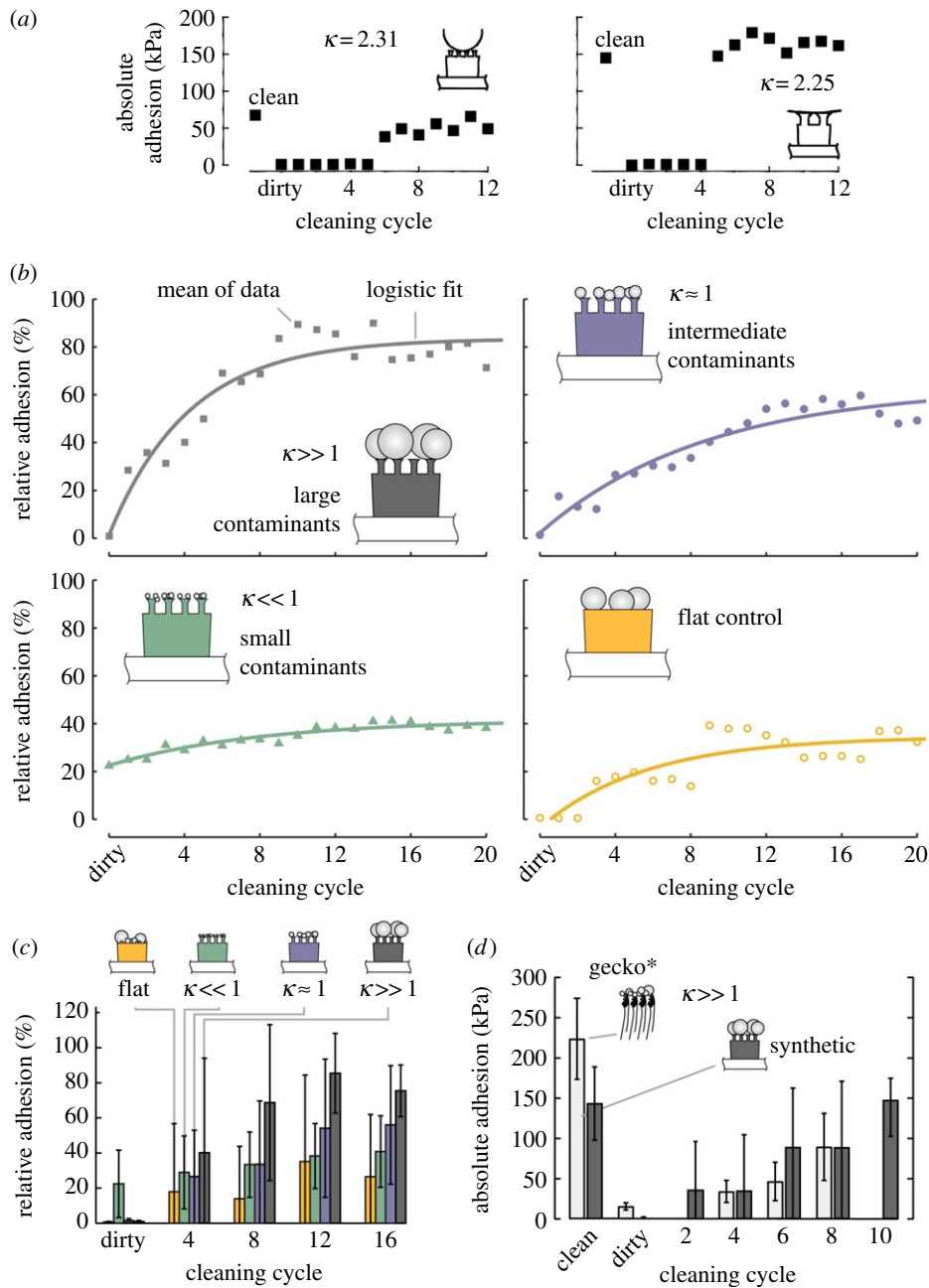


**Figure 5.** Cleaning experiment results for the large, intermediate and small contaminants regimes and comparison with the cleaning performance of the natural gecko. (a) Comparison of the adhesion recovery curves for two representative samples in the large contaminants regime ( $\kappa > 2$ ) shows similar recovery trends although the samples and contaminants dimensions are significantly different. (b) Graph of *relative adhesion* after various cleaning cycles for all three contaminants regimes and the flat sample. The solid line is obtained from the function  $P_{ad}(t) = F_{ad} - c \exp(-t/T)$  that was fitted to the data as a guide to the eye and to predict the steady-state *relative adhesion* values for each regime. The results show that samples in the large contaminants regime had the best adhesion recovery performance followed by the intermediate and small contaminants regime. The flat sample had the least adhesion recovery. In addition, the samples in the small contaminants regime had the highest *relative adhesion* immediately after contamination and, therefore, showed the best *contamination resistance*. The insets are representative diagrams of the contaminant regimes (see figure 2 for all combinations of fibre and particle diameters in each regime). (c) Adhesion recovery performance of samples in all three contamination regimes and the flat control for the first 16 cleaning cycles clearly shows the exceptional self-cleaning performance of the large contaminants regime (dark grey bars) and the *contamination resistance* of the small contaminants regime (green bars). (d) A comparison of the best recovery case of synthetic fibrillar adhesives (95  $\mu\text{m}$  tip diameter fibres with 215  $\mu\text{m}$  diameter particles) with the natural gecko (data from reference [8]) shows that, in some cases, our synthetic adhesive could match the gecko's adhesion and cleaning performance. (Online version in colour.)

Owing to the random population and position of the contaminants in each samples, the processes of adhesion recovery for two samples were never alike. Nevertheless, we observed a general agreement between the adhesion recovery trend for a given contaminant size regime, depending on the ratio of the particle diameter to the fibre tip diameter. In figure 5a, for example, we compared the adhesion recovery curves of two very different dimensions

of the fibre and contaminants. The left graph shows the absolute adhesion values for a sample with  $B = 20 \mu\text{m}$  and  $D = 46.2 \mu\text{m}$  ( $D/B = 2.31$ ), whereas the right graph shows the same type of data for a sample with a much larger tip diameter ( $B = 95 \mu\text{m}$ ) and particle diameter ( $D = 213.6 \mu\text{m}$ ), but with  $D/B = 2.25$ . Despite the differences in the sample sizes and in the absolute adhesion values (67.2 kPa for the small fibres and 144.5 kPa for the large fibres), the two curves

**Table 1.** Fitting parameters for the three different self-cleaning regimes.

	$c$	$T$
$\kappa \gg 1$ ( $\kappa > 2$ )	81.2	4.3
$\kappa \approx 1$ ( $0.75 \leq \kappa \leq 2$ )	61.3	9.1
$\kappa \ll 1$ ( $\kappa < 0.75$ )	19.2	8.3
flat	38.2	5.6

have very similar trends and show a *relative adhesion* of nearly 100% after only four to six cleaning cycles. Therefore, we defined the ratio between the contaminant diameter and the fibre diameter as an important non-dimensional parameter,  $\kappa = D/B$ . Consequently, we identified three regimes of contaminant sizes (figure 2). In the *large contaminants regime*, the diameter of the contaminating particles is much larger than the tip diameter, i.e.  $\kappa \gg 1$ . In the *small contaminants regime*, the diameter of the contaminating particle is much smaller than the fibre tip diameter ( $\kappa \ll 1$ ). In the *intermediate contaminants regime*, the value of  $\kappa$  is approximately 1. This classification of regimes allowed us to directly compare different fibre and contaminant sizes. In the experiments, we approximated the small and large contaminants regimes as  $\kappa < 0.75$  and  $\kappa > 2.0$  cases, respectively. The solid lines shown in figure 4b are based on the fitting function  $P_{ad}(t) = F_{ad} - c \exp(-t/T)$ , and serves as a guide to the eye and to predict the steady-state recovered adhesion for each regime, where  $P_{ad}$  represents the percentage of *clean adhesion*,  $F_{ad}$  is the limit of adhesion recovery,  $c$  and  $T$  are the fitting coefficients and  $t$  is the number of cleaning cycles. Table 1 shows the values of the fitting parameters  $c$  and  $T$  that were computed for the different contaminants regimes.

### 3.1. Cleaning mechanisms

The experiments revealed two mechanisms of contact self-cleaning, namely: *deposition*, during which particles are transferred to the contacted substrate (figure 4b), and *embedding*, during which the particles are lodged between adjacent microfibrils or fibre patches (figure 4c). Thus, the mechanism of adhesion recovery is not necessarily that of actually removing contaminants from the adhesive. Such definition expands on previous studies, which only considered particles much greater in diameter than the fibres and proposed contact self-cleaning only by deposition [8,26,35]. Contaminant embedding is also observed in the natural gecko. The principal goal of the gecko is to recover adhesion as fast as possible, which can be achieved by simply removing contaminants from the tips of the adhesive structures. The contaminant's destination in a short time scale is not critical for the effectiveness of the gecko's toe as well as synthetic adhesives. However, it is important to note that particle embedding is only a temporary cleaning process, hence the shedding of the gecko's skin every two months. For embedding to take place between adjacent fibres, the particle diameter must be smaller than the fibre length,  $L$  (figure 6b), and the particle diameter must be smaller than the fibre spacing,  $S$  (figure 6c).

### 3.2. Contamination resistance

We investigated the ability of the microfibre arrays to remain adhesive immediately after contamination; we call this

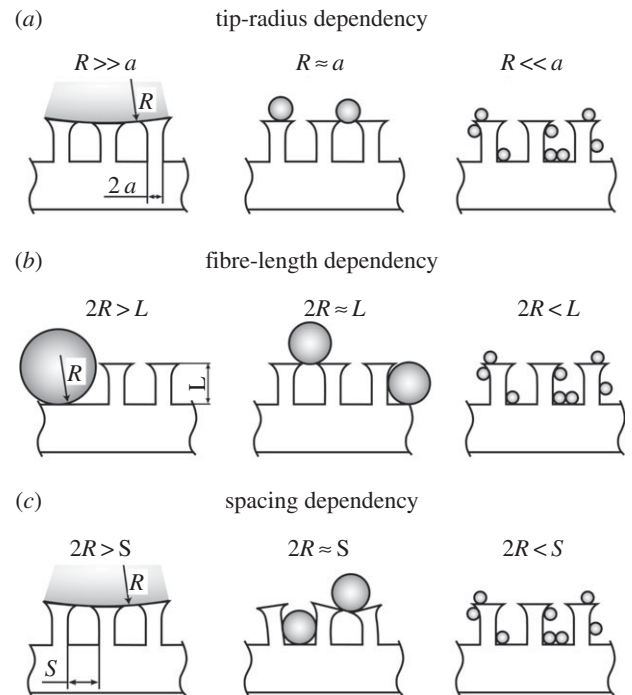


**Figure 6.** Parameters that influence dry contact self-cleaning performance for a fibrillar adhesive include: (a) the fibre tip radius, (b) the length of the microfibrils, and (c) the spacing between fibres.  $a$  is the fibre tip radius,  $R$  is the particle radius,  $L$  is the fibre length and  $S$  is the fibre spacing.

phenomenon *contamination resistance*. The *dirty adhesion*, i.e. adhesion measurements directly after contamination and before the first cleaning cycle, shows insignificant *contamination resistance* for the samples in the large and intermediate contaminants regimes. These samples lost almost all of their initial adhesion upon contamination, because the contaminating particles were so large that the fibres could barely make contact with the substrate. However, adhesion dropped to 22.4% immediately after contamination for the samples in the small contaminants regime (figure 5c), indicating a significant *contamination resistance*. Three possible explanations are presented for the observed *contamination resistance* of the small particle regime, namely: the random distribution of contaminants across the sample, the mechanics of the mushroom-shaped fibre tip [36,37] and the adhesion contribution of the small contaminants to the overall adhesive force of the array. In the first case, although the contaminants form a monolayer, they are stochastically distributed across the array such that some fibres retain clean tips after contamination. For the second case, even when a fibre tip is contaminated, the mushroom-shaped tip can deform around the contaminating particle and make good contact during loading as long as the contaminants are much smaller than the fibre tip [38,39]. Lastly, the adhesive force of several contaminating particles making contact with the substrate can add up significantly and contribute to the overall adhesion of the sample.

To further understand the contribution of particle adhesion to the overall adhesion of a contaminated sample, we developed a model of adhesion of a non-contaminated and a contaminated array for various  $\kappa$ -values. Consider a microfibre array where all microfibrils have mushroom tips and are of equal height such that they make contact simultaneously with a flat substrate. Assuming that the substrate is atomically smooth and very rigid, the adhesive force of a

**Table 2.** Simulation result for adhesion of a non-contaminated microfibre array,  $P_{nc}$ , and adhesion of contaminated fibre arrays,  $P_c$ , contaminated with large microsphere contaminants ( $\kappa > 2$ ) and small microsphere contaminants ( $\kappa < 0.75$ ). Small microsphere contaminants result in up to 21.1% relative adhesion compared with the non-contaminated array, whereas larger microspheres result in as low as 0.56% relative adhesion. Note that these results are for the maximum number of contaminants in the array. In practice, the number of contaminating particles could be less, resulting in larger reduction of the adhesive force.

$a$ ( $\mu\text{m}$ )	$n$	$\sigma_s$ (MPa)	$P_{nc}$ (mN)	$P_c$ ( $\kappa = 10.7$ ) (mN) $B = 213.6 \mu\text{m}$ ; $N = 4$	$P_c$ ( $\kappa = 5.9$ ) (mN) $B = 118.5 \mu\text{m}$ ; $N = 16$	$P_c$ ( $\kappa = 0.1$ ) (mN) $B = 2.8 \mu\text{m}$ ; $N = 11\ 560$
10	289	0.29	26.33	$0.15 \pm 0.01$	$0.33 \pm 0.01$	$5.56 \pm 0.90$

non-contaminated microfibre array,  $P_{nc}$ , with  $n$  number of microfibrils can be given as

$$P_{nc} = n\sigma_s\pi a^2, \quad (3.1)$$

where  $\sigma_s$  is the adhesive strength of an individual microfibre, and  $a$  is the tip radius of the fibre. For a fully contaminated array where none of the fibres are in contact with the substrate, we assume that the contaminating particles are all of approximate radius (similar to the experiment), so that all the particles are in contact. The resulting contaminated array will have adhesive force,  $P_c$ , determined by the total particle–substrate adhesion given by

$$P_c = \sum_{i=1}^N 2\pi W_{ps} R(i), \quad (3.2)$$

where  $R(i)$  is the radius of the  $i$ th particle,  $W_{ps}$  is the work of adhesion at the particle–substrate interface, and  $N$  is the number of particles on the microfibre array that are in contact with the substrate. Here, the Derjaguin–Muller–Toporov (DMT) model [40] is used to model adhesion owing to rigid–rigid interactions between the rigid particles and substrate, and very small Tabor parameter. For a  $500 \times 500 \mu\text{m}$  adhesive patch consisting of 289 small-sized elastomer polyurethane microfibrils ( $D = 20 \mu\text{m}$ , stem diameter =  $10 \mu\text{m}$ , fibre spacing =  $20 \mu\text{m}$ ,  $W_{fs} = 93 \text{ mJ m}^{-2}$  and  $\sigma_s = 0.29 \text{ MPa}$  from experiments), the *clean adhesion* of a non-contaminated array on a glass substrate can be obtained from equation (3.1) as 26.33 mN. If the array is contaminated by small silica microspheres ( $B = 2.8 \mu\text{m}$ ,  $W_{ps} = 56 \text{ mJ m}^{-2}$ ), the adhesive force obtained from equation (3.2) is 5.56 mN, which is 21.1% of the *clean adhesion*. On the other hand, if the array is contaminated by large microspheres ( $B = 118.5 \mu\text{m}$ ), the adhesive force becomes 0.33 mN, which is 1.25% of the *clean adhesion*. For even larger microspheres ( $B = 213.6 \mu\text{m}$ ), the adhesive force is 0.15 mN and 0.6% of the *clean adhesion*. The results in table 2 show that, for a fully contaminated sample, small contaminants contribute much to the adhesion of the sample compared with large contaminants. The theoretical result of the *relative adhesion* immediately after contamination with small particles matches closely with that of the experiments. The model result for large contaminants also supports the data from the cleaning experiments.

### 3.3. Adhesion recovery

Figure 5b shows the average adhesion recovery as a function of the cleaning cycles for all three contaminants size regimes. From the graphs, the large contaminants regime has the highest adhesion recovery followed by the intermediate and small contaminants regimes. Adhesion recovery in the large contaminants regime saturated at 80% after nine cleaning cycles with  $N = 5$  tested samples. In the intermediate

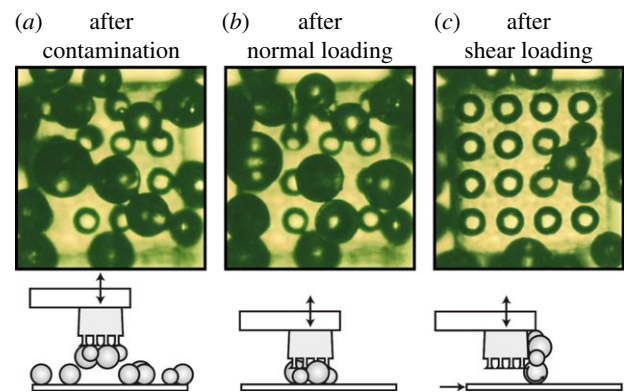


**Figure 7.** Micrographs showing a large microfibre sample contaminated with particles with mean diameter of  $118.5 \mu\text{m}$ ; (a) after contamination, (b) after normal loading and unloading and (c) after shear loading. The result presented here as well as those of other samples investigated ( $N = 15$ ) showed that 95% of particles were cleaned during shear loading (s.d. = 13%), which indicates that shearing is a key process in dry contact cleaning. (Online version in colour.)

contaminants regime, the adhesion reached 55% of *clean adhesion* in only 12 cleaning cycles ( $N = 6$ ). The adhesion recovery saturated to 40% for the small contaminants regime in 11 cleaning cycles ( $N = 8$ ). For the flat control sample, we found that only very large particles could be cleaned. The overall performance of the control was worse than that of all the fibre samples, with adhesion recovery of approximately 35% after 20 cleaning cycles ( $N = 5$ ). The poor adhesion recovery for the small contaminants regime and the control samples is due to the fibre tip making contact with the substrate during the cleaning steps. When this occurs, the fibre tip does not move laterally relative to the substrate even when dragging, so that particle sliding or rolling is inhibited. This condition is easily reached after the first few cleaning cycles for the small contaminants regime, such that no further cleaning is observed in subsequent steps even though some contaminants are present on the fibre tip (see SEM image of the small contaminants in figure 4d).

### 3.4. Effect of normal and shear loading

To investigate how the loading mode affects particle cleaning, we counted the particles removed from the samples during normal and shear loading steps in some of the experiments where the particles were larger than  $40 \mu\text{m}$ . Figure 7 shows micrographs of a large microfibre sample contaminated with particles with mean diameter of  $118.5 \mu\text{m}$  after contamination (a), after normal loading and unloading (b) and after shear loading (c). We observed that 95% of the particles removed were cleaned during the shear loading and the remainder during the normal loading (s.d. = 13%,  $N = 15$ ). The result suggests that particle rolling or sliding across the

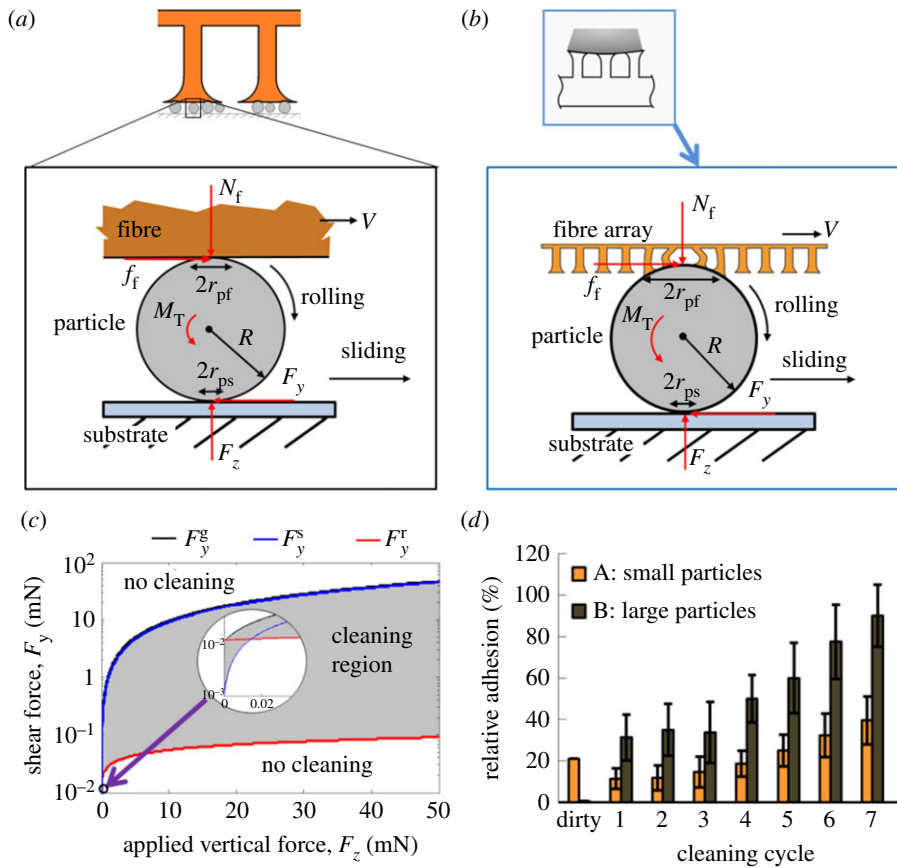


**Figure 8.** Loading conditions for a single particle sandwiched between a fibre array and a glass substrate during the load–drag–unload cleaning processes for the small contaminants regime (a) and the large contaminants regime (b).  $F_y$  and  $F_z$  are the applied shear force and the vertical load, respectively,  $f_f$  and  $f_g$  are the friction and  $r_{pf}$  and  $r_{ps}$  are the contact radii at the fibre–particle and the substrate–particle interfaces, respectively,  $N_f$  is the normal reaction force at the fibre–particle interface,  $M_T$  is the rolling resistance and  $V$  is the dragging speed. (c) Contact self-cleaning map for a 150  $\mu\text{m}$  diameter glass particle in the small contaminants regime shows the vertical and lateral load values that result in contact self-cleaning (grey region) by particle rolling or sliding, predicted by equation (3.11).  $F_y^g$  (black line),  $F_y^s$  (blue line) and  $F_y^r$  (red line) represent the critical shear forces required for the particle to slide with respect to the glass substrate, slide with respect to the fibre surface and roll on both surfaces, respectively. The graph shows that the particle behaviour during dragging motion would be dominated by rolling when  $F_z > 0.015$  mN and by sliding along the fibre interface otherwise. (d) Simulation results of dry contact cleaning using a load–drag–unload procedure for small (samples A) and large (samples B) contaminants regimes. The simulation result shows trends that are very similar to the experimental results in figure 5c, both for adhesion recovery and contamination resistance. Each bar represents the mean and standard deviation of 20 simulations conducted for randomly generated sets of particles each with the same mean and standard deviation. (Online version in colour.)

contact interface dominates the dry contact cleaning process. Although the dragging step is very important for the cleaning of the adhesives, it also posed a challenge to the lifetime of the fibres. In some cases, the shear force required for cleaning had the potential to damage the adhesive, a danger also present in the natural gecko [8]. We have not investigated the effects of repeated shear loading, but other researchers have presented possible material or geometrical options that could improve the longevity of gecko-inspired adhesives [41].

To further understand the contributions of normal and shear loading to dry contact cleaning of fibrillar adhesives, we developed an approximate model that shows the mechanics of a rigid spherical contaminant sandwiched between a soft flat microfibre tip and a rigid flat substrate, when a normal and shear load is applied. In the model, we assume that all surfaces are smooth, and that the microfibrils deform linearly under small load. The current model is for the small and large contaminants regime only. The mechanics of a normal loading is first presented, followed by the mechanics of normal and shear loading which results in either sliding or rolling of the particle. Figure 8 shows the forces acting on the contaminants in the small and large

contaminants regimes. In the diagram,  $F_y$  and  $F_z$  are the applied shear force and the vertical load, respectively,  $f_f$  and  $f_g$  are the frictional force and  $r_{pf}$  and  $r_{ps}$  are the contact radii at the fibre–particle and the substrate–particle interfaces, respectively,  $N_f$  is the normal reaction force at the fibre–particle interface,  $M_T$  is the rolling resistance and  $V$  is the dragging speed.

In the small contaminants regime (figure 8a), cleaning occurs under normal loading when a particle is transferred from the fibre tip onto a contacted substrate. In this case, the adhesive force at the particle–substrate interface,  $P_{ps}$ , must be greater than the adhesive force at the particle–fibre interface,  $P_{pf}$ , such that

$$P_{pf} < P_{ps}, \quad (3.3)$$

where  $P_{pf} = 1.5\pi W_{pf}R$  is obtained from the Johnson–Kendall–Roberts (JKR) model [42] for the contact of a hard sphere with a soft elastomer, and  $P_{ps} = 2\pi W_{ps}R$  is obtained from the DMT model for contact of a hard sphere with a hard substrate. The subscripts ‘ps’ and ‘pf’ refer to the particle–substrate and particle–fibre interfaces, respectively,  $W$  is the work of adhesion of the interfaces and  $R$  is the radius

of the particle. Substituting for  $P_{pf}$  and  $P_{ps}$  in equation (3.3) shows that, under only normal load, cleaning occurs when

$$W_{ps} > \frac{3}{4} W_{pf}. \quad (3.4)$$

Equation (3.4) is not satisfied in the case of experiments with a rigid glass substrate. For rigid contaminants in contact with soft elastomer fibres, equation (3.4) is typically not satisfied except in contact with a specially designed tacky substrate. Therefore, dragging is a crucial step in the cleaning process.

During dragging, the particle can slide across either the fibre or the substrate surface, or roll on both surfaces. For cleaning to take place by sliding, the particle should not move relative to the substrate, but must slide relative to the fibre tip. For the particle to be stationary relative to the substrate,  $F_y$  must be less than the critical shear force  $F_{ps}$  required for the particle to slide on the particle–substrate interface given by

$$F_{ps} = \tau_{ps}(\pi r_{ps}^2) + \mu_{ps} F_z, \quad (3.5)$$

where  $\tau$  is the interfacial shear strength,  $\mu$  is the coefficient of friction and  $r$  is the contact radius of the interface. On the other hand, for the particle to slide on the fibre surface,  $F_y$  must be greater than or equal to the critical shear force  $F_{pf}$  of the particle–fibre interface given by

$$F_{pf} = \tau_{pf}(\pi r_{pf}^2) + \mu_{pf} F_z. \quad (3.6)$$

In equations (3.5) and (3.6), the first term accounts for the constant friction stress, and the second term accounts for the Coulomb friction contributions at the interfaces. The constant friction stress dominates for soft contact interfaces, whereas the Coulomb friction contribution dominates for hard contact interfaces. In the case of our experiments, the second term will dominate in equation (3.5) for the hard particle–substrate interface, whereas the first term will dominate in equation (3.6) for a soft particle–fibre interface. The contact radius for each interface can be obtained from the JKR and DMT contact models for the soft particle–fibre and hard particle–substrate interfaces, respectively, as

$$r_{pf}^3 = \frac{R}{E_{pf}^*} \left( F_z + 3W_{pf}\pi R + \sqrt{6W_{pf}\pi R F_z + (3W_{pf}\pi R)^2} \right) \quad (3.7)$$

and

$$r_{ps}^3 = \frac{R}{E_{ps}^*} (F_z + 2W_{ps}\pi R), \quad (3.8)$$

where  $1/E_{12}^* = 3/4[(1 - \nu_1^2)/E_1 + (1 - \nu_2^2)/E_2]$ ,  $E$  is the Young's modulus and  $\nu$  is the Poisson ratio of the respective contacting surfaces noted by subscripts 1 and 2. Based on experimental and theoretical values of reported shear strength at different scales of contact radii, Sumer & Sitti [43] have shown that  $\tau$  decreases as the contact size increases, except for very small contact radii (less than 20 nm) and large contact radii (larger than 40  $\mu\text{m}$ ), and is given as

$$\tau_{12} = \begin{cases} G_{12}/43, & r_{12} < 20 \text{ nm}, \\ G_{12}10^Q \left(\frac{r_{12}}{b}\right)^M, & 20 \text{ nm} < r_{12} < 40 \mu\text{m}, \\ G_{12}/1290, & r_{12} > 40 \mu\text{m}, \end{cases} \quad (3.9)$$

where  $M = \tan^{-1}[(G_{12}/43 - G_{12}/1290)/(8 \times 10^4 - 28)b]$ ,  $Q = 28b$ ,  $b = 0.5 \text{ nm}$  is the Burgers vector,  $G_{12} = 2G_1G_2/(G_1 + G_2)$ ,  $G_1$  and  $G_2$  are the shear moduli of the materials, and  $G_i = E_i/2(1 + \nu_i)$ .

For cleaning by particle rolling, the moment owing to the applied shear force (i.e.  $2F_yR$ ) must be greater than the total rolling resistance  $M_T$  from both contact interfaces. By calculating the approximate pressure distribution of the shifted (asymmetric) contact geometry of rolling particles using the JKR model, Dominik & Tielens [44] derived the rolling resistance  $M$  between two particles as  $M = 6\pi RW\xi$ , where  $\xi$  is the critical rolling distance before the contact radius readjusts. In their work, Dominik and Tielens accounted for both the work done in opening the region in the wake of the rolling contact, and the work done by the adhesive forces ahead of the rolling contact. The value of  $\xi$  ranges from the interatomic distance  $\varepsilon$  to the contact radius such that  $\varepsilon \leq \xi \leq r$ . In the present analysis, we assume a conservative approximation such that  $\xi = r$ . The total rolling resistance for a particle sandwiched between two surfaces is obtained by summing the rolling resistances of both contact interfaces, and is given as

$$M_T = 6\pi R(W_{pf}\xi_{pf} + W_{ps}\xi_{ps}). \quad (3.10)$$

Combining equations (3.5), (3.6) and (3.10), the conditions for a sliding- or rolling-based particle cleaning under shear loading can be given as

$$\tau_{ps}(\pi r_{ps}^2) + \mu_{ps} F_z > F_y \geq \begin{cases} \tau_{pf}(\pi r_{pf}^2) + \mu_{pf} F_z & \text{sliding,} \\ 3\pi(W_{pf}\xi_{pf}(F_z) + W_g\xi_g(F_z)) & \text{rolling.} \end{cases} \quad (3.11)$$

The above model is applied to a glass particle with  $D = 46.2 \mu\text{m}$ , Young's modulus  $E_p = 73 \text{ GPa}$ , Poisson's ratio  $\nu_p = 0.17$ , friction coefficient with glass  $\mu_{ps} = 0.9$  and work of adhesion with substrate  $W_{ps} = 56 \text{ mJ m}^{-2}$ . The particle is sandwiched between a glass substrate and a single elastomer fibre with  $B = 95 \mu\text{m}$ , fibre length  $L = 105 \mu\text{m}$ , fibre edge-to-edge spacing  $S = 75 \mu\text{m}$ , Young's modulus  $E_f = 2.9 \text{ MPa}$ , Poisson's ratio  $\nu_f = 0.49$ , friction coefficient with glass  $\mu_{pf} = 0.9$  [45] and the interfacial work of adhesion between the fibre and particle  $W_{pf} = 93 \text{ mJ m}^{-2}$ . Figure 8c shows a shear-based cleaning map obtained from equation (3.11) using the above parameters.  $F_y^g$ ,  $F_y^s$  and  $F_y^r$  represent the critical shear forces required for the particle to slide with respect to the glass substrate, or slide with respect to the fibre surface, or roll on both surfaces, respectively, for an applied normal load of up to 50 mN. The graph shows that cleaning can occur by sliding or rolling, where particle sliding across the fibre dominates when  $F_z < 15 \mu\text{N}$ , particle rolling dominates for  $F_z > 15 \mu\text{N}$ , and the particle can be cleaned by rolling with slipping at  $F_z = 15 \mu\text{N}$ . Thus, because  $F_z > 15 \mu\text{N}$  during the experiments and in the simulations, cleaning in the small particles regime is dominated by particle rolling. However, depending on the system parameters, particle sliding along the fibre surface or particle deposition to the substrate could also dominate the cleaning process.

In the large contaminants regime (figure 8b), the particle is significantly larger than the fibre tip such that many fibres can be in contact with the particle simultaneously. Here, the condition for contact cleaning under normal loading is similar to the small contaminants regime. But unlike the case for small particles, the adhesive force of the particle–fibre interface is more complex to compute, because the contacting fibres have different and independent tension or compression behaviour during loading and unloading.

Second, the number of contacting fibres is dependent on the applied preload force. Therefore, the preload-dependent pull-off force in the large contaminants regime is numerically obtained from simulation as the maximum tensile force when unloading [35]. As a result, the cleaning condition under normal load is dependent on the particle size, the applied preload force as well as the work of adhesion of the particle–fibre and particle–substrate interfaces.

To model cleaning owing to shear loading in the large contaminants regime, the fibre array can be approximated as an elastic foundation. Such approximation was previously proposed by Persson [46]. Consequently, the cleaning condition for small contaminants in equation (3.11) can be directly applied for large particles except for changes to some parameters. First, the total normal force exerted on the fibre array by a single particle can be obtained by integrating the deformation  $\delta$  of all the contacting fibres in contact, and multiplying the result by the stiffness  $k$  of a single fibre, i.e.  $F_z = \int k\delta_i dn$ , where  $n$  is the number of fibres in contact. Solving the equation, we obtain the force at a given indentation distance of the sample  $\Delta$  as

$$F_z = \pi\rho kR\Delta^2. \quad (3.12)$$

It is important to note that  $F$  is linearly proportional to  $R$  and the square of  $\Delta$ , unlike the Hertzian relationship where  $F$  is proportional to  $R^{1/2}$  and  $\Delta^{3/2}$ . Second, the contact radius between a particle and the fibre array is obtained from equation (3.12) as

$$r_{\text{pf}}^4 = \frac{4FR}{\pi\rho k}, \quad (3.13)$$

which is used in place of equation (2.7) as the contact radius of the particle–fibre interface.

The model developed is applied to a numerical simulation of dry contact cleaning using a load–drag–unload procedure for small and large contaminants regimes. The simulation result in figure 8*d* shows trends that are very similar to the experimental results, for both adhesion recovery and contamination resistance. Each bar in the result represents the mean and standard deviation of 20 simulations conducted for randomly generated sets of particle sizes.

### 3.5. Comparison of the self-cleaning performance of the synthetic and the natural gecko adhesives

In addition to a good adhesion recovery performance, it is important for the adhesive to attach strongly in both clean and cleaned states. We analysed the absolute adhesion of the microfibrils and observed that the large microfibrils with 95  $\mu\text{m}$  tip diameter had the highest *clean adhesion* among our tested adhesives, with up to 35 mN of attachment force (140 kPa for the 500  $\times$  500  $\mu\text{m}$  patch). Interestingly, the large microfibrils in the large contaminants regime were comparable in absolute adhesion and contact self-cleaning performance to the natural gecko (figure 5*d*). In making this comparison, it is important to note the differences and similarities in the test protocols between our study and natural gecko self-cleaning studies [7,8]. First, our observations were for a patch area smaller than a single gecko toe, and as the patch size increases, the observed adhesive performance may decrease [28]. Second, the cleaning procedures for the gecko and for our synthetic fibres involved shearing of the adhesive along a clean glass surface. In both studies, the contaminants were particles in the large

contaminants regime. Additionally, the contaminants were spheres in both cases, but ceramic for one of the gecko studies [8] and glass in this study. The geometry and material stiffness of the natural and synthetic adhesives are different, but the effective modulus of the surfaces is similar (gecko  $\approx$  100 kPa [47], 95  $\mu\text{m}$  tip diameter fibres  $\approx$  30 kPa, determined empirically). Lastly, the adhesive performance, in this study, was characterized in normal pulling, but in the shear direction for the gecko studies. Despite some of these differences, the principal comparison is valid, and, for the first time, we demonstrate a synthetic adhesive that is as sticky on a flat substrate and as effective at regaining adhesion through contact self-cleaning as the gecko.

Biological and some synthetic [12] micro/nanofibrillar adhesives have angled fibre stems and angled spatulated tips, which enable controllability and directionality to adhesion and friction behaviour at the fibre–substrate interface. Such structures would also have some differences during load–drag–unload-based contact self-cleaning. First, during vertical loading only, angled structures with angled tips would be more compliant vertically and would not make full tip contact with the contaminants or the substrate without dragging in the gripping direction, which would reduce their contamination possibility and require different loading conditions for self-cleaning. Next, during dragging, the direction of dragging would affect the contaminant cleaning performance, because the fibre stiffness and tip contact would be different in the ‘gripping’ and ‘releasing’ directions [12]; it is expected that it would be easier to clean the asymmetric fibres in the ‘releasing’ direction. Therefore, although the demonstrated rolling- and sliding-based self-cleaning mechanics would apply to the gecko fibres too, biological fibre stem bending and fibre tip contact behaviour would differ as a function of loading and directional dragging, which would add more variables to the cleaning models and experiments. A study of contact self-cleaning of directional fibrils is a future work.

## 4. Design implications

### 4.1. Fibre tip radius

From our experiments, the large contaminants regime had the least *contamination resistance* but had the fastest adhesion recovery rate as well as the highest *relative adhesion* after only eight cleaning cycles (figure 5*b*). The result shows that cleaning of fibrillar adhesive is most efficient when the fibril tip diameter is much smaller than that of the contaminating particle. This finding suggests that the nanometre size of the gecko’s spatulae not only improves adhesion by the contact splitting principle [4], but also guarantees that its adhesive pad is in the large contaminants regime for superior adhesion recovery. Thus, when designing a synthetic fibrillar adhesive for contact self-cleaning, it is important to make the microfibrils much smaller than the contaminants that are predominant in its application environment, for enhanced adhesion recovery.

In contrast, the small contaminants regime showed the best *contamination resistance* with a high *relative adhesion* immediately after contamination and before the first cleaning cycle. This result is particularly useful in situations where cleaning of the adhesives (using the load–drag–unload process or any other effective cleaning procedure) is not desired or cannot be implemented. In such cases, the best practice

will be the design of adhesives that are robust to contamination. Therefore, fibrillar adhesives with fibril tips that are larger than the predominant contaminants present in the application environment are desired.

## 4.2. Design of adhesive patch with grooves

Our results also showed that particle embedding is a predominant cleaning mechanism compared with deposition. Apart from dynamic cleaning processes such as digital hyperextension [7], other known dry contact cleaning processes require specialized surfaces with higher adhesion strength than the adhesive in order to achieve cleaning by deposition. As a result, cleaning by contaminant embedding should be seriously considered for both short-term and long-term cleaning of fibrillar adhesives. The natural gecko has evolved to possess skin folds called lamellae at the base of its fibrillar structures. These lamellae folds help to enhance self-cleaning in the gecko as it create cavities for contaminants to be embedded for a longer period of time, before it can regenerate its skin. Similarly, we propose that fibrillar adhesives with grooves mimicking the lamellae in the gecko are more efficient for particle embedding and, consequently, enhanced contact self-cleaning performance.

To further strengthen our hypothesis that grooves can enhance dry contact cleaning, and to qualitatively test the principle, we created an adhesive patch with lamellae-like grooves (figure 4*e–j*). The patch was patterned into rows of microfibrils on raised ridges with equal gaps (figure 4*e*). The mushroom-tipped microfibrils used for the patterned patch were 95  $\mu\text{m}$  in tip diameter. The patch was patterned such that the raised ridges were four pillars wide (550  $\mu\text{m}$ ) and the intervening gaps were two pillars wide (225  $\mu\text{m}$ ), resulting in approximately 67% area coverage of adhesive structures. Using only manual manipulation of the adhesive patch, we demonstrated that, even after contamination by glass spheres with  $D = 110 \mu\text{m}$ , the lamellae-patterned patch could be cleaned enough to recover 17% of the uncontaminated adhesion after 10 steps (figure 4*g*). The lamellae-patterned adhesive patch (figure 4*h*) performed far better than its non-patterned counterpart (figure 4*i*).

Overall, the lamellae-inspired grooves allowed for embedding of various-sized particles and led to some adhesion recovery. However, a limitation to the current design is an uneven shear pressure across the surface of the adhesive patch, causing the leading edges of the ridges to experience greater stresses, and resulting in damage to the adhesive. The

lamellae-inspired design can be further improved in future work to reduce the stress concentration issues through optimized design of the grooves and/or by mimicking the slanted lamellae design of the natural gecko adhesive pad. It is also important to note that, as the grooves get filled up with particles, the contaminants begin to make contact with the substrate. Consequently, further cleaning is inhibited. This observation reaffirms that, despite the increase in the effectiveness and longevity of embedding through the groove design, embedding remains a temporary cleaning measure. The adhesives can be replaced when the grooves are saturated.

## 5. Conclusion

We have presented experiments and approximate models for the contact self-cleaning of gecko-inspired elastomer microfibre adhesives with mushroom-shaped tips. We observed a significant adhesive recovery greater than that of previously reported synthetic fibrillar adhesive both in attachment strength (140 kPa) and in the percentage of recovered adhesion (up to 100%) on a smooth substrate. These observations show that our synthetic gecko adhesives could recover from adhesion loss upon contamination at a rate comparable to that of the gecko. Our study of the mechanics of contact self-cleaning leads us to conclude that embedding of contaminants between adjacent fibres or lamellae-inspired grooves, by particle rolling, is an important mechanism of contact self-cleaning for elastomeric gecko adhesives. Consequently, a rational design of lamellae-like grooves will be beneficial for contact self-cleaning, as demonstrated in our proof-of-concept results. Furthermore, we observed that the relative size of the contaminants to the size of the microfibre tips in an array of synthetic adhesive strongly determined how and to what degree the adhesive could be cleaned. Future works will include the characterization of real-world contaminants with different materials, geometries and sizes, modelling and characterization of directional (angled) fibrillar adhesives, and the development of more advanced numerical contact cleaning models.

**Acknowledgements.** We thank T. Novitsky, P. Glass, B. Aksak, E. Cheung, P. Abaffy, J. Weaver, J. Leuthold and V. Saile for their help.

**Funding statement.** M.S. and Y.M. were supported by the NSF CMMI-1130520 grant. U.A. was supported by the NSF Graduate Student Fellowship under grant no. 0946825. M.R. thanks the Karlsruhe House of Young Scientists for funding this collaboration.

## References

- Autumn K *et al.* 2002 Evidence for van der Waals adhesion in gecko setae. *Proc. Natl Acad. Sci. USA* **99**, 12 252–12 256. (doi:10.1073/pnas.192252799)
- Gao H, Yao H. 2004 Shape insensitive optimal adhesion of nanoscale fibrillar structures. *Proc. Natl Acad. Sci. USA* **101**, 7851–7856. (doi:10.1073/pnas.0400757101)
- Autumn K *et al.* 2000 Adhesive force of a single gecko foot-hair. *Nature* **405**, 681–685. (doi:10.1038/35015073)
- Arzt E, Gorb SN, Spolenak R. 2003 From micro to nano contacts in biological attachment devices. *Proc. Natl Acad. Sci. USA* **100**, 10 603–10 606. (doi:10.1073/pnas.1534701100)
- Tian Y, Pesika N, Zeng H, Rosenberg K, Zhao B, McGuiggan P, Autumn K, Israelachvili J. 2006 Adhesion and friction in gecko toe attachment and detachment. *Proc. Natl Acad. Sci. USA* **103**, 19 320–19 325. (doi:10.1073/pnas.0608841103)
- Glassmaker NJN, Jagota A, Hui C-Y, Noderer WL, Chaudhury MK. 2007 Biologically inspired crack trapping for enhanced adhesion. *Proc. Natl Acad. Sci. USA* **104**, 10 786–10 791. (doi:10.1073/pnas.0703762104)
- Hu S, Lopez S, Niewiarowski PH, Xia Z. 2012 Dynamic self-cleaning in gecko setae via digital hyperextension. *J. R. Soc. Interface* **9**, 2781–2790. (doi:10.1098/rsif.2012.0108)
- Hansen WW, Autumn K. 2005 Evidence for self-cleaning in gecko setae. *Proc. Natl Acad. Sci. USA* **102**, 385–389. (doi:10.1073/pnas.0408304102)
- Ge L, Sethi S, Ci L, Ajayan PM, Dhinojwala A. 2007 Carbon nanotube-based synthetic gecko tapes. *Proc. Natl Acad. Sci. USA* **104**, 10 792–10 795. (doi:10.1073/pnas.0703505104)

10. Geim AK, Dubonos SV, Grigorieva IV, Novoselov KS, Zhukov AA, Shapoval SY. 2003 Microfabricated adhesive mimicking gecko foot-hair. *Nat. Mater.* **2**, 461–463. (doi:10.1038/nmat917)
11. Kim S, Sitti M. 2006 Biologically inspired polymer microfibers with spatulate tips as repeatable fibrillar adhesives. *Appl. Phys. Lett.* **89**, 261911. (doi:10.1063/1.2424442)
12. Murphy MP, Aksak B, Sitti M. 2009 Gecko-inspired directional and controllable adhesion. *Small* **5**, 170–175. (doi:10.1002/smll.200801161)
13. Qu L, Dai L, Stone M, Xia Z, Wang ZL. 2008 Carbon nanotube arrays with strong shear binding-on and easy normal lifting-off. *Science* **322**, 238–242. (doi:10.1126/science.1159503)
14. Murphy M, Kim S, Sitti M. 2009 Enhanced adhesion by gecko-inspired hierarchical fibrillar adhesives. *ACS Appl. Mater. Interfaces* **1**, 849–855. (doi:10.1021/am8002439)
15. Kim S, Cheung E, Sitti M. 2009 Wet self-cleaning of biologically inspired elastomer mushroom shaped microfibrillar adhesives. *Langmuir* **25**, 7196–7199. (doi:10.1021/la900732h)
16. Kim S, Aksak B, Sitti M. 2007 Enhanced friction of polymer microfiber adhesives with spatulate tips. *Appl. Phys. Lett.* **91**, 221 913–221 915. (doi:10.1063/1.2820755)
17. Sitti M, Fearing RS. 2003 Synthetic gecko foot-hair micro/nano-structures as dry adhesives. *J. Adhes. Sci. Technol.* **17**, 1055–1074. (doi:10.1163/156856103322113788)
18. Sitti M, Cusick B, Aksak B, Nese A, Lee H, Dong H, Kowalewski T, Matyjaszewski K. 2009 Dangling chain elastomers as repeatable fibrillar adhesives. *ACS Appl. Mater. Interfaces* **1**, 2277–2287. (doi:10.1021/am9004368)
19. Glass P, Chung H, Washburn NR, Sitti M. 2010 Enhanced wet adhesion of elastomeric micro-fiber arrays with mushroom tip geometry and a photopolymerized p(DMA-co-MEA) tip coating. *Langmuir* **26**, 17 357–17 362. (doi:10.1021/la1029245)
20. Aksak B, Hui CY, Sitti M. 2011 Effect of aspect ratio on adhesion for soft elastic fibers. *J. R. Soc. Interface* **8**, 1166–1175. (doi:10.1098/rsif.2010.0582)
21. Kim S, Sitti M, Xie T, Xiao X. 2009 Reversible dry adhesives with thermally controllable adhesion. *Soft Matter* **5**, 3689–3693. (doi:10.1039/b909885b)
22. Aksak B, Sitti M, Cassell A, Li J, Meyyappan M, Callen P. 2007 Friction of partially embedded vertically aligned carbon nanofibers inside elastomers. *Appl. Phys. Lett.* **91**, 061 906–061 908. (doi:10.1063/1.2767997)
23. Murphy M, Aksak B, Sitti M. 2007 Adhesion and anisotropic friction enhancement of angled heterogeneous micro-fiber arrays with spherical and spatula tips. *J. Adhes. Sci. Technol.* **21**, 1281–1296. (doi:10.1163/156856107782328380)
24. Sethi S, Ge L, Ci L, Ajayan PM, Dhinojwala A. 2008 Gecko-inspired carbon nanotube-based self-cleaning adhesives. *Nano Lett.* **8**, 822–825. (doi:10.1021/nl0727765)
25. Lee J, Fearing RS. 2008 Contact self-cleaning of synthetic gecko adhesive from polymer microfibers. *Langmuir* **24**, 10 587–10 591. (doi:10.1021/la8021485)
26. Gillies AG, Puthoff J, Cohen MJ, Autumn K, Fearing RS. 2013 Dry self-cleaning properties of hard and soft fibrillar structures. *ACS Appl. Mater. Interfaces* **5**, 6081–6088. (doi:10.1021/am400839n)
27. Kwak MK, Jeong HE, Suh KY. 2011 Rational design and enhanced biocompatibility of a dry adhesive medical skin patch. *Adv. Mater.* **23**, 3949–3953. (doi:10.1002/adma.201101694)
28. Asbeck AT *et al.* 2009 Climbing rough vertical surfaces with hierarchical directional adhesion. In *Proc. IEEE Int. Conf. on Robotics and Automation (ICRA '09), Kobe, Japan, 12–17 May 2009*, pp. 2675–2680. Piscataway, NJ: IEEE.
29. Murphy MP, Kute C, Mengüç Y, Sitti M. 2010 Waalbot II: adhesion recovery and improved performance of a climbing robot using fibrillar adhesives. *Int. J. Robot Res.* **30**, 118–133. (doi:10.1177/0278364910382862)
30. Mengüç Y, Yang SY, Kim S, Rogers JA, Sitti M. 2012 Gecko-inspired controllable adhesive structures applied to micromanipulation. *Adv. Funct. Mater.* **22**, 1246–1254. (doi:10.1002/adfm.201101783)
31. Jeong HE, Lee J-K, Kim HN, Moon SH, Suh KY. 2009 A nontransferring dry adhesive with hierarchical polymer nanohairs. *Proc. Natl Acad. Sci. USA* **106**, 5639–5644. (doi:10.1073/pnas.0900323106)
32. Karp JM, Langer R. 2011 Materials science: dry solution to a sticky problem. *Nature* **477**, 42–43. (doi:10.1038/477042a)
33. Lee J, Fearing RS, Komvopoulos K. 2008 Directional adhesion of gecko-inspired angled microfiber arrays. *Appl. Phys. Lett.* **93**, 191910. (doi:10.1063/1.3006334)
34. Aksak B, Murphy MP, Sitti M. 2007 Adhesion of biologically inspired vertical and angled polymer microfiber arrays. *Langmuir* **23**, 3322–3332. (doi:10.1021/la062697t)
35. Hui CY, Shen L, Jagota AJ, Autumn K. 2006 Mechanics of anti-fouling or self-cleaning in gecko setae. In *Proc. 29th Annual Meeting of the Adhesion Society, Inc., Jacksonville, Florida, 19–22 February 2006*, pp. 29–31. Blacksburg, VA: Adhesion Society.
36. Carbone G, Pierro E, Gorb SN. 2011 Origin of the superior adhesive performance of mushroom-shaped microstructured surfaces. *Soft Matter* **7**, 5545–5552. (doi:10.1039/c0sm01482f)
37. Spuskanyuk AV, McMeeking RM, Deshpande VS, Arzt E. 2008 The effect of shape on the adhesion of fibrillar surfaces. *Acta Biomater.* **4**, 1669–1676. (doi:10.1016/j.actbio.2008.05.026)
38. Persson BNJ. 2007 Biological adhesion for locomotion on rough surfaces: basic principles and a theorist's view. *Mater. Res. Soc. Bull.* **32**, 486–490. (doi:10.1557/mrs2007.82)
39. Hui CY, Jagota A, Shen L, Rajan A, Glassmaker N, Tang T. 2007 Design of bio-inspired fibrillar interfaces for contact and adhesion: theory and experiments. *J. Adhes. Sci. Technol.* **21**, 1259–1280. (doi:10.1163/156856107782328362)
40. Derjaguin BV, Muller VM, Toporov Y. 1975 Effect of contact deformations on the adhesion of particles. *J. Colloid Interface Sci.* **53**, 314–326. (doi:10.1016/0021-9797(75)90018-1)
41. Gillies AG, Fearing RS. 2011 Shear adhesion strength of thermoplastic gecko-inspired synthetic adhesive exceeds material limits. *Langmuir* **27**, 11 278–11 281. (doi:10.1021/la202085j)
42. Johnson KL, Kendall K, Roberts AD. 1971 Surface energy and contact of elastic solids. *Proc. R. Soc. Lond. A* **324**, 301–313. (doi:10.1098/rspa.1971.0141)
43. Sumer B, Sitti M. 2008 Rolling and spinning friction characterization of fine particles using lateral force microscopy based contact pushing. *J. Adhes. Sci. Technol.* **22**, 481–506. (doi:10.1163/156856108X295527)
44. Dominik C, Tielens AGGM. 1995 Resistance to rolling in the adhesive contact of two elastic spheres. *Phil. Mag. A* **72**, 783–803. (doi:10.1080/01418619508243800)
45. Piccardo M, Chateauinois A, Fretigny C, Pugno NM, Sitti M. 2013 Contact compliance effects in the frictional response of bioinspired fibrillar adhesives. *J. R. Soc. Interface* **10**, 20130182. (doi:10.1098/rsif.2013.0182)
46. Persson BNJ. 2003 On the mechanism of adhesion in biological systems. *J. Chem. Phys.* **118**, 7614–7621. (doi:10.1063/1.1562192)
47. Autumn K *et al.* 2006 Frictional adhesion: a new angle on gecko attachment. *J. Exp. Biol.* **209**, 3569–3579. (doi:10.1242/jeb.02486)